J|A|C|S ARTICLES

Published on Web 08/31/2010

Enzymatic Ring-Opening Mechanism of Verdoheme by the Heme Oxygenase: A Combined X-ray Crystallography and QM/MM Study

Wenzhen Lai,[†] Hui Chen,[†] Toshitaka Matsui,[‡] Kohei Omori,[‡] Masaki Unno,[‡,§] Masao Ikeda-Saito,*[,‡] and Sason Shaik*[,†]

Institute of Chemistry and The Lise Meitner-Minerva Center for Computational Quantum Chemistry, The Hebrew University of Jerusalem, 91904 Jerusalem, Israel, and Institute of Multidisciplinary Research for Advanced Materials, Tohoku University, Katahira, Sendai, 980-8577, Japan

Received May 29, 2010; E-mail: sason@yfaat.ch.huji.ac.il; mis2@tagen.tohoku.ac.jp

Abstract: The least understood mechanism during heme degradation by the enzyme heme oxygenase (HO) is the third step of ring opening of verdoheme to biliverdin, a process which maintains iron homeostasis. In response to this mechanistic uncertainty, we launched a combined study of X-ray crystallography and theoretical QM/MM calculations, designed to elucidate the mechanism. The air-sensitive ferrous verdoheme complex of HmuO, a heme oxygenase from *Corynebacterium diphtheriae*, was crystallized under anaerobic conditions. Spectral analysis of the azide-bound verdoheme−HmuO complex crystals assures that the verdoheme group remains intact during the crystallization and X-ray diffraction measurement. The structure offers *the first solid evidence for the presence of a water cluster in the distal pocket of this catalytically critical intermediate*. The subsequent QM/MM calculations based on this crystal structure explore the reaction mechanisms starting from the FeOOH−verdoheme and FeHOOH−verdoheme complexes, which mimic, respectively, the O_2- and H_2O_2-supported degradations. In both mechanisms, the rate-determining step is the initial O−O bond breaking step, which is either homolytic (for FeHOOH−verdoheme) or coupled to electron and proton transfers (in FeOOH−verdoheme). Additionally, the calculations indicate that the FeHOOH−verdoheme complex is more reactive than the FeOOH−verdoheme complex in accord with experimental findings. QM energies with embedded MM charges are close to and yield the same conclusions as full QM/MM energies. Finally, *the calculations highlight the dominant influence of the distal water cluster which acts as a biocatalyst for the conversion of verdoheme to biliverdin in the two processes*, by fixing the departing OH and directing it to the requisite site of attack, and by acting as a proton shuttle and a haven for the highly reactive OH^- nucleophile.

1. Introduction

Heme oxygenases (HOs) are key enzymes, which are in charge of iron recovery and of the generation of the neurotransmitter CO molecule. Thus, these enzymes use O_2 and catalyze the degradation of heme to biliverdin, CO, and a free iron ion, through a process in which the heme group participates as both the prosthetic group and substrate, Scheme 1.[1−4] It is known that heme degradation by HO proceeds through three successive steps of O_2 activation: (i) the regiospecific self-hydroxylation of the porphyrin α-*meso* position to form α-*meso*-hydroxyheme; (ii) conversion of hydroxyheme to verdoheme and CO; and (iii) the cleavage of the verdoheme macrocycle to release biliverdin and free ferrous iron.[3−5] The mechanism of the first step has been extensively studied by both experimental[6−9] and theoretical[10−14] means and is better understood now. The third step, the ring opening of verdoheme, which is considered to be the

[†] The Hebrew University of Jerusalem.
[‡] Tohoku University.
[§] Present address: Frontier Research Center for Applied Atomic Sciences, Ibaraki University, Tokai, Ibaraki 319-1106, Japan.

(1) Ortiz de Montellano, P. R.; Wilks, A. *Adv. Inorg. Chem.* **2001**, *51*, 359–407.
(2) Colas, C.; Ortiz de Montellano, P. R. *Chem. Rev.* **2003**, *103*, 2305–2332.
(3) Unno, M.; Matsui, T.; Ikeda-Saito, M. *Nat. Prod. Rep.* **2007**, *24*, 553–570.
(4) Matsui, T.; Unno, M.; Ikeda-Saito, M. *Acc. Chem. Res.* **2010**, *43*, 240–247.
(5) Wilks, A. *Antioxid. Redox Signal.* **2002**, *4*, 603–614.
(6) Wilks, A.; Ortiz de Montellano, P. R. *J. Biol. Chem.* **1993**, *268*, 22357–22362.
(7) Wilks, A.; Torpey, J.; Ortiz de Montellano, P. R. *J. Biol. Chem.* **1994**, *269*, 29553–29556.
(8) Liu, Y.; Moene-Loccoz, P.; Loehr, T. M.; Ortiz de Montellano, P. R. *J. Biol. Chem.* **1997**, *272*, 6909–6917.
(9) Chu, G. C.; Katakura, K.; Zhang, X.; Yoshida, T.; Ikeda-Saito, M. *J. Biol. Chem.* **1999**, *274*, 21319–21325.
(10) Kamachi, T.; Shestakov, A. F.; Yoshizawa, K. *J. Am. Chem. Soc.* **2004**, *126*, 3672–3673.
(11) Kamachi, T.; Yoshizawa, K. *J. Am. Chem. Soc.* **2005**, *127*, 10686–10692.
(12) Sharma, P. K.; Kevorkiants, R.; de Visser, S. P.; Kumar, D.; Shaik, S. *Angew. Chem., Int. Ed.* **2004**, *43*, 1129–1132.
(13) Kumar, D.; de Visser, S. P.; Shaik, S. *J. Am. Chem. Soc.* **2005**, *127*, 8204–8213.
(14) Chen, H.; Moreau, Y.; Derat, E.; Shaik, S. *J. Am. Chem. Soc.* **2008**, *130*, 1953–1965.

 10.1021/ja104674q

Scheme 1. Three Steps in the Degradation of Heme Catalyzed by HO[a]

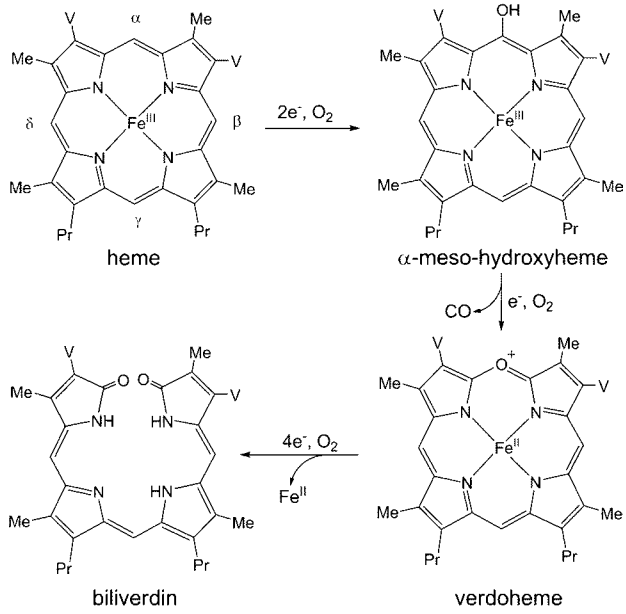

[a] Me: $-CH_3$; V: $-CH{=}CH_2$; Pr: $-CH_2-CH_2CO_2H$.

Scheme 2. Possible Resonance Structures of Ferrous Verdoheme[a]

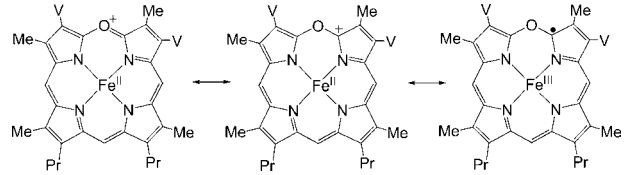

[a] Me: $-CH_3$, V: $-CH{=}CH_2$; Pr: $-CH_2-CH_2CO_2H$.

rate-limiting step in the HO activity,[15] is the most intriguing and enigmatic step, which we attempt herein to understand by combined experiment and theory.

Verdoheme can be nonenzymatically converted to biliverdin (BV) by hydrolysis or by redox reactions using O_2 or H_2O_2.[16−18] Early reports showed that the HO enzyme exclusively utilizes O_2 for BV formation,[19] whereas H_2O_2 did not support the verdoheme degradation by HO.[6] However, a recent study[20] revealed that for ferrous verdoheme, but not the ferric complex, HO degrades verdoheme through a dual pathway using either O_2 or H_2O_2 and the H_2O_2 reaction is about 50 times faster than the O_2 reaction. Additionally, the binding of O_2 or H_2O_2 was found to be the rate-determining step, and corresponding mechanisms were then proposed.[20] Thus, based on the resonance forms of Fe(II)−verdoheme in Scheme 2, H_2O_2 binding may occur either on the verdoheme iron or at the partially cationic α-pyrrole carbon. The two binding modes will produce the Fe−OOH or ring-OOH verdoheme intermediate complexes,

Scheme 3. Three Possible Pathways for the Verdoheme Ring Opening by HO Using H_2O_2 (blue) and ROOH (Red) as Oxygen Sources

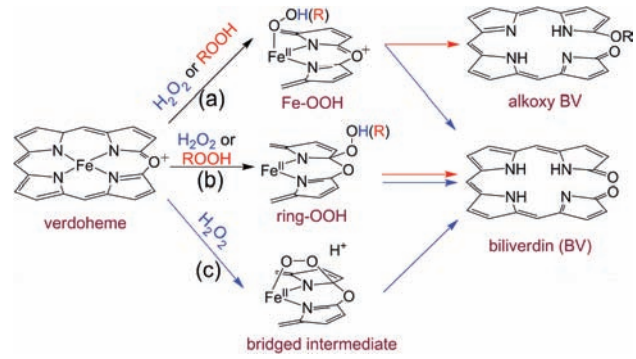

which are shown in (a) and (b) in Scheme 3. These two species may in turn undergo deprotonation to form a bridged intermediate (see pathway (c) in Scheme 3). Subsequently, upon O−O bond cleavage, all three possible intermediates could potentially generate BV. Do they all coexist, or is one of them dominant? This was the question.

To discriminate the three possible pathways, the Sendai group has recently studied the reaction of a verdoheme−HO-1 complex with alkyl hydroperoxides,[21] which yields the corresponding alkoxy-biliverdin. The study suggested that the bridged and ring-OOR species are not intermediates in the process, because for the bridged case, the liberation of the alkyl group is prohibitive, while the ring-OOR case could be dismissed because the reaction actually produced alkoxy BV instead of the expected normal BV. These exclusions leave the Fe−OOR species as the only possible intermediate (among (a)−(c) in Scheme 3) during the alkyl hydroperoxide supported reaction. Still however, for the H_2O_2-dependent reaction itself, the possibility of the bridged intermediate could not be ruled out since here deprotonation is possible. Thus, the identity of the complex that mediates the H_2O_2-supported reaction is still unknown.

Another dilemma concerns the role of the protein residues. The distal Asp140 was found to play a major role in the degradation to BV,[20] like in the *meso*-hydroxylation initial step. Mutations of Asp140 in rat HO-1 cause a significant decrease in the yields of BV in the O_2 and H_2O_2-dependent verdoheme degradations.[20] Hence, Asp140 is likely to play an important role in the O−O activation by the verdoheme. As such, the mechanism may be similar to the one[12−14] proposed for the first oxygenation by HO, *meso*-hydroxylation of heme, wherein, by analogy with the first step, the Fe−OOH moiety in the verdoheme complex can possibly interact with the nearby water cluster in the pocket, which is stabilized by the distal Asp140 residue. The immense importance of the water cluster was demonstrated before by the Jerusalem group, using quantum mechanical/molecular mechanical (QM/MM) calculations.[14] However, this analogy is enigmatic for the degradation to BV, because the crystal structure of the pentacoordinated Fe(II)−verdoheme−human HO-1 complex[22] does not show water in the distal heme pocket, while, for the hexacoordinated low-spin Fe(II)−verdoheme having either water or hydroxide as a

(15) Liu, Y.; Ortiz de Montellano, P. R. *J. Biol. Chem.* **2000**, *275*, 5297–5307.
(16) Fuhrhop, J. H.; Kruger, P. *Liebigs. Ann. Chem.* **1977**, 360–370.
(17) Saito, S.; Itano, H. A. *Proc. Natl. Acad. Sci. U.S.A.* **1982**, *79*, 1393–1397.
(18) Sano, S.; Sano, T.; Morishima, I.; Shiro, Y.; Maeda, Y. *Proc. Natl. Acad. Sci. U.S.A.* **1986**, *83*, 531–535.
(19) Docherty, J. C.; Schacter, B. A.; Firneisz, G. D. *J. Biol. Chem.* **1984**, *259*, 13066–13069.
(20) Matsui, T.; Nakajima, A.; Fujii, H.; Mansfiled Matera, K.; Migita, C. T.; Yoshida, T.; Ikeda-Saito, M. *J. Biol. Chem.* **2005**, *280*, 36833–36840.
(21) Matsui, T.; Omori, K.; Jin, H.; Ikeda-Saito, M. *J. Am. Chem. Soc.* **2008**, *130*, 4220–4221.
(22) Lad, L.; Ortiz de Montellano, P. R.; Poulos, T. L. *J. Inorg. Biochem.* **2004**, *98*, 1686–1695.

sixth ligand,[23,24] such a water cluster might exist. A recent crystal structure work reported the presence of a water cluster in the rat verdoheme−HO-1 complex, but the verdoheme group in the crystal used was modified as evidenced by the finding that the absorption spectrum of the crystal was quite different from that of the authentic Fe(II) verdoheme−HO complex.[25] As such, the existence of a water cluster in the Fe(II) verdoheme−HO complex still requires proof.

To resolve the structural and mechanistic uncertainties of the third oxidation step in the HO catalysis, we have decided to launch a combined study of X-ray crystallography and QM/MM calculations. The crystallographic study was performed on a heme oxygenase from *Corynebacterium diphtheriae*, HmuO, whose amino acid sequence has significant homology to those of mammalian HOs (identity: ∼34%), especially in the active site region (identity: ∼76%).[26] HmuO and mammalian HOs are similar in both their reaction mechanisms and crystal structures.[27,28] Since the instability of the oxy-verdoheme[20] precluded its crystallization, the stable azide-bound verdoheme complex of HmuO was used as a model for the oxy form. The azide ligand binds to the heme iron of heme proteins in a bent end-on geometry as in the case of dioxygen binding to heme proteins. The crystallography of this complex indeed revealed the presence of six water molecules. The subsequent QM/MM mechanistic exploration based on this HO crystal structure confirms the proposed reaction mechanism and highlighted once again the paramount importance of the water cluster, for the execution of the third oxidation step by HO, and the power of combined experiment and theory in resolving mechanistic issues.

2. Experimental and Computational Methods

2.1. Experimental Part. 2.1.1. Crystallization of Azide-Bound Fe(II)−Verdoheme−HmuO. Reconstitution and purification of Fe(II)−verdoheme−HmuO were performed by a method described earlier[20] with a slight modification. The purified HmuO protein[29] was incubated with 2 mol equiv. of verdoheme in a Vacuum Atomospher Nexus anaerobic glovebox at 2 °C for 12 h. The mixture was passed through a short DEAE cellulose (Whatman DE52) column equilibrated with 0.3 M potassium phosphate (pH 7.0), 0.1 M KCl to remove excess verdoheme, followed by gel filtration on Sephadex G-25 for buffer exchange to 20 mM MES, pH 7.0. The purified verdoheme−HmuO complex with an Abs(399 nm)/Abs(280 nm) value of 1.2 was concentrated to 18 mg/mL.

The verdoheme−HmuO crystals were grown anaerobically in the glovebox at approximately 30 °C by a hanging drop vapor diffusion method. The protein stock solution was mixed to generate drops with an equal volume of a reservoir solution containing 50 mM MES (pH 5.4), 2.3−2.5 M ammonium sulfate, 0.27 M sodium bromide, and 0.1% dioxane. Green needle-like crystals were soaked in a cryo-protectant solution (50 mM MES (pH 5.4), 2.5 M ammonium sulfate, and 25% sucrose) containing 10 mM sodium azide for 20 min. The single crystals of the azide-bound form of the verdoheme−HmuO complex were flash-frozen in the glovebox by liquid nitrogen.

2.1.2. X-ray Data Collection. X-ray diffraction data of the azide bound verdoheme−HmuO complex was collected with an ADSC Quantum 270 CCD detector using 1.0 Å synchrotron radiation on beamline BL17A at the Photon Factory, Tsukuba, Japan. The temperature around the crystals was maintained at 100 K throughout the data collection. The oscillation angle, camera distance, and exposure time were 1.0°, 183 mm, and 3.0 s, respectively. The data set consisted of 180 frames. The data were integrated, merged, and processed with HKL-2000.[30] Data collection conditions and diffraction data statistics are summarized in Table S1 in the Supporting Information (SI). Optical absorption spectra of the crystals before and after the X-ray diffraction data collection were recorded using a microspectrophotometer (4DX Systems AB, Uppsala, Sweden) in the visible region at 100 K.

2.1.3. Structure Determination and Refinement. The structure of the azide-bound verdoheme−HmuO complex was solved by a molecular replacement method using the structure of the ferrous verdoheme−HmuO complex, the structure of which had been determined earlier[31] as an initial model. Rigid-body refinement was performed using program CNS[32] with the structure factor in the 15−3.0 Å range. The phase was gradually extended with noncrystallographic restraints between two molecules in an asymmetric unit to 1.70 Å resolution. The crystallographic refinements with simulated annealing, individual B factor refinements by CNS, and manual model correction by Coot[33] were repeated. In the course of the refinement, water molecules were added to the model. The model was further refined using the program REFMAC5.[34] After including additional water molecules, alternative conformations for several residues were introduced. Refinement statistics are summarized in Table S1. Atomic coordinates and structural factors have been deposited in the Protein Data Bank under accession numbers of 3MOO.

2.2. Computational Study. 2.2.1. Setup of the System. Only one monomer from the asymmetric unit of the so determined X-ray structure was used, corresponding to the protein chain A in which the first six amino acids, which are unresolved, were omitted in the calculations. The sucrose and sulfate anions were removed. The distally bound azide was replaced by OOH (HOOH) groups. Hydrogen positions were added at pH 7 on the basis of CHARMM internal coordinates with the HBUILD facility[35] and then optimized by the CHARMM force field[36] as implemented in the CHARMM program[37] (3600 steps of steepest descent for all hydrogen atoms). The pK_a values of the titratable residues were estimated by PKOPKA[38,39] at pH 7. Using PROPKA, the pK_a values of His25, His150, His162, and His192 suggest that these are doubly protonated residues. Additionally, after a closer inspection of the PDB file, the histidines His20, His128, His129, and His205 were protonated at the ε-nitrogen only. The additions of protons at these positions would form reasonable hydrogen bonds to acceptors nearby. Moreover, aspartates (Asp) and glutamates (Glu) were used as negatively charged, and arginines (Arg) and lysines (Lys) were used as positively charged. The total charge of the so-generated system was −7. Then a 16-Å thick water solvent layer was

(23) Takahashi, S.; Mansfiled Matera, K.; Fujii, H.; Zhou, H.; Ishikawa, K.; Yoshida, T.; Ikeda-Saito, M. *Biochemistry* **1997**, *36*, 1402–1410.
(24) Damaso, C. O.; Bunce, R. A.; Barybin, M. V.; Wilks, A.; Rivera, M. *J. Am. Chem. Soc.* **2005**, *127*, 17582–17583.
(25) Sato, H.; Sugishima, M.; Sakamoto, H.; Higashimoto, Y.; Shimokawa, C.; Fukuyama, K.; Palmer, G.; Noguchi, M. *Biochem. J.* **2009**, *419*, 339–345.
(26) Schmitt, M. P. *J. Bacteriol.* **1997**, *179*, 838–845.
(27) Chu, G. C.; Katakura, K.; Zhang, X.; Yoshida, T.; Ikeda-Saito, M. *J. Biol. Chem.* **1999**, *274*, 21319–21325.
(28) Unno, M.; Matsui, T.; Chu, G. C.; Couture, M.; Yoshida, T.; Rousseau, D. L.; Olson, J. S.; Ikeda-Saito, M. *J. Biol. Chem.* **2004**, *279*, 21055–21061.
(29) Matsui, T.; Furukawa, M.; Unno, M.; Tomita, T.; Ikeda-Saito, M. *J. Biol. Chem.* **2005**, *280*, 2981–2989.
(30) Otwinowski, Z.; Minor, W. *Methods Enzymol.* **1997**, *276*, 307–326.
(31) Matsui, T.; Unno, M.; Ikeda-Saito, M. Unpublished results.
(32) Brunger, A. T.; et al. *Acta Cystallogr., Sect. D: Biol. Crystallogr.* **1998**, *54*, 905–921.
(33) Emsley, P.; Cowtan, K. *Acta Cystallogr., Sect. D: Biol. Crystallogr.* **2004**, *60*, 2126–2132.
(34) Bailey, S. *Acta Cystallogr., Sect. D: Biol. Crystallogr.* **1994**, *50*, 760–763.
(35) Bruger, A. T.; Karplus, M. *Proteins* **1988**, *4*, 148–156.
(36) MacKerell, A. D., Jr.; et al. *J. Phys. Chem. B* **1998**, *102*, 3586–3616.
(37) Brooks, B. R.; Bruccoleri, R. E.; Olafson, B. D.; States, D. J.; Swaminathan, S.; Karplus, M. *J. Comput. Chem.* **1983**, *4*, 187–217.
(38) Li, H.; Robertson, A. D.; Jensen, J. H. *Proteins* **2005**, *61*, 704–721.
(39) Bas, D. C.; Rogers, D. M.; Jensen, J. H. *Proteins* **2008**, *73*, 765–783.

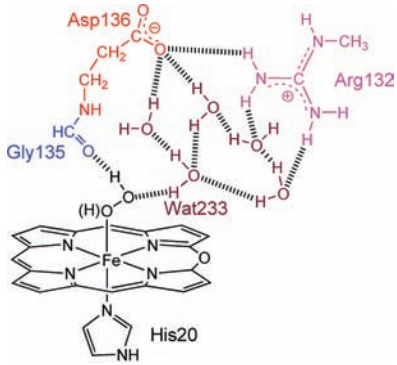

Figure 1. QM region used in this work.

constructed around the enzyme. The inner layer of 8 Å of water was then processed through a procedure involving (i) MM optimization for 2400 steps, (ii) heating to 300 K, (iii) equilibration for 3 ps, and (iv) a second optimization for 2400 steps. This procedure of adding the solvent was repeated once to ensure that not more than 100 additional water molecules were added. The entire system consists of 15 358 atoms, including 11 508 atoms in the solvent. For the iron hydrogen peroxide species, a proton was added to the proximal oxygen atom.

2.2.2. QM/MM Methodology and Software. QM/MM calculations were done with ChemShell,[40] combining Turbomole[41]/DL_POLY.[42] An electronic embedding scheme[43] was applied to include the polarizing effect of the enzyme environment on the QM region. Hydrogen link atoms with the charge shift model[44] were used to treat the QM/MM boundary. The CHARMM22 force field[36] was used throughout this study for the MM part. For geometry optimization, the hybrid B3LYP functional[45−48] and two basis sets were used. The first one, labeled as B1a, involves 6-31+G(d) for the iron-coordinated O_2 molecule and the O atom in Wat233, a double-ζ basis set LACVP[49] for iron, and 6-31G for all other atoms. B1a was used for the O−O bond breaking and HO transfer steps. The second basis set, labeled as B1b, involves 6-31+G(d) for four oxygen and two carbon atoms, i.e., O_2, O in Wat233, and the O and adjoined two carbon on the ring (see Figure 1), a double-ζ basis set LACVP for iron, and 6-31G for all other atoms. The latter basis set was used in the steps after the formation of FeO(H) hydroxyl-verdoheme species (see Figure 1). In all cases, the energy was corrected by single-point calculations with a larger basis set B2, involving Def-TZVP[50] for all the atoms. We also tested the B3LYP with a dispersion correction[51] (B3LYP-D), using single-point energies at the B2 level with Gaussian09.[52] We found that all the conclusions remained intact. These results are relegated to the SI.

B3LYP has been repeatedly shown to be capable of reproducing both experimental and high-level calculation results for heme systems.[53] However, in the particular case of the binding of oxygen to heme groups, B3LYP shows a large deviation from the experimental results, due to a lack of both multireference and van der Waals effects.[54] In order to test the system with a more suitable functional for this case, we also considered the B3LYP* functional,[55] where the exact exchange in B3LYP is decreased from 20% to 15%. The single-point B3LYP* calculations were carried out at the B2 level using Gaussian09 on the key species in the rate-limiting steps. B3LYP*-D results, which include dispersion corrections, were also obtained and are given and relegated to the SI.

2.2.3. QM Region. As shown in Figure 1, the QM region comprises a (H)OOH-bound ferrous verdoheme complex (without side chains of verdoheme) with its proximal ligand His20 (modeled as imidazole) and a few key protein residues: Arg132 (modeled as $CH_3NHC^+(NH_2)_2$), Asp136 (modeled as $NHCH_2CH_2COO^-$), and Gly135 (HCO), including five crystal waters that form a water cluster through a hydrogen-bond network in the distal pocket.

2.2.4. Optimized QM/MM Region. The QM/MM optimized region is similar to the one in our previous work,[14] and it included the following set of residues: Lys13, Thr16, Ala19, His20 (including verdoheme), Glu21, Ala23, Glu24, Met29, Leu33, Gln46, Tyr53, Tyr130, Val131, Arg132, Tyr133, Leu134, Gly135, Asp136, Leu137, Ser138, Gly139, Gly140, Gln141, Val142, Ile143, Ala144, Phe160, Tyr161, Arg177, Phe201, Phe208; some crystal waters: Wat232, Wat233, Wat234, Wat235, Wat238, Wat250, Wat252, Wat262, Wat273, Wat285, Wat288, Wat303, Wat360; and solvent waters: Solv2256, Solv2262, Solv2270, Solv2272, Solv2275, Solv2296, Solv2317, Solv2334, Solv2360, Solv2372.

Due to the size of the optimized region, it is important to ascertain that mechanisms possess contiguous energy curves by going forward and backward in a given scan. This was done here, and all the mechanistic steps, with two exceptions, were found to be contiguous. In the first case, which involves a long-range electron transfer process, a single-reference DFT calculation leads to state crossing. However, this was found to have no consequences. For example, in the triplet O−O bond breaking in the FeOOH pathway, the difference between the barriers for forward and backward scans is 0.6 kcal/mol (17.8 and 17.2 kcal/mol). This difference is so small that we estimate the activation energy from the forward scan. In the second case, which involves O−C bond formation (in the FeOOH pathway), there is also a proton transfer from O_{dist} to Wat233, whose degree of freedom is not covered by the scanning coordinate. Therefore, we performed a two-dimensional (2D) scan by adding the proton transfer reaction coordinate as a second dimension and, hence, estimated the activation energy from the 2D scan; again the difference compared to the 1D scan was within 0.5 kcal/mol. The full set of data, including all tried mechanisms, are summarized in the SI, while herein we focus on the key results.

3. Results

3.1. Crystal Structure of the Azide-Bound Verdoheme−HmuO Complex. The single crystals of the azide bound form of verdoheme−HmuO were prepared and manipulated under strictly anaerobic conditions to avoid air oxidation of the reactive verdoheme intermediate. The verdoheme group remains intact during the crystallization process as shown by negligible changes in the absorption spectra (Figure S1a in the SI). The spectra of the single crystals were typical of the azide-bound verdoheme and were essentially the same as those taken after the X-ray diffraction measurements (Figure S1b in the SI), indicating no adverse radiation damage during the data collection. These spectral data thus indicate that the diffraction data are originated

(40) Sherwood, P.; et al. *J. Mol. Struct. (THEOCHEM)* **2003**, *632*, 1–28.
(41) Ahlrichs, R.; Bär, M.; Häser, M.; Horn, H.; Kölmel, C. *Chem. Phys. Lett.* **1989**, *162*, 165–169.
(42) Smith, W.; Forester, T. R. *J. Mol. Graph.* **1996**, *14*, 136–141.
(43) Bakowies, D.; Thiel, W. *J. Phys. Chem.* **1996**, *100*, 10580–10594.
(44) de Vries, A. H.; Sherwood, P.; Collins, S. J.; Rigby, A. M.; Rigutto, M.; Kramer, G. J. *J. Phys. Chem. B* **1999**, *103*, 6133–6141.
(45) Becke, A. D. *Phys. Rev. A* **1988**, *38*, 3098–3100.
(46) Lee, C.; Yang, W. T.; Parr, R. G. *Phys. Rev. B* **1988**, *37*, 785–789.
(47) Becke, A. D. *J. Chem. Phys.* **1993**, *98*, 5648–5652.
(48) Becke, A. D. *J. Chem. Phys.* **1993**, *98*, 1372–1377.
(49) Hay, P. J.; Wadt, W. R. *J. Chem. Phys.* **1985**, *82*, 299–310.
(50) Schäfer, A.; Huber, C.; Ahlrichs, R. *J. Chem. Phys.* **1994**, *100*, 5829–5835.
(51) Grimme, S. *J. Comput. Chem.* **2006**, *27*, 1787–1799.
(52) Frisch, M. J.; et al. *Gaussian 09*, revision A.02; Gaussian Inc.: Wallingford, CT, 2009.
(53) Shaik, S.; Cohen, S.; Wang, Y.; Chen, H.; Kumar, D.; Thiel, W. *Chem. Rev.* **2010**, *110*, 949–1017.
(54) Siegbahn, P. E. M.; Blomberg, M. R. A.; Chen, S.-L. *J. Chem. Theory Comput.* **2010**, *6*, 2040–2044.
(55) Reiher, M.; Salomon, O.; Hess, B. A. *Theor. Chem. Acc.* **2001**, *107*, 48–55.

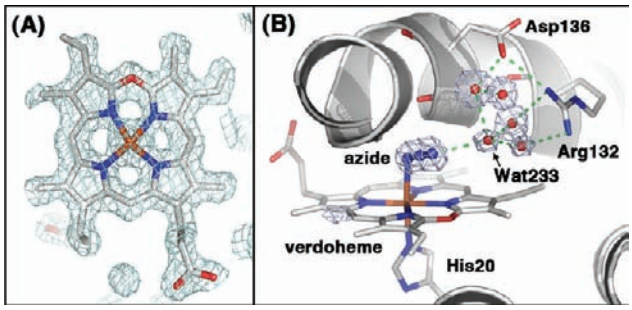

Figure 2. Active site structures of the azide-bound verdoheme−HmuO complex determined at 1.7 Å resolution (molecule A). (A) A $2F_o-F_c$ map (1.2σ) around verdoheme moiety. (B) An F_o-F_c map (3.8σ) calculated from a structural model lacking the azide ligand and water molecules in the active site.

from the azide-bound Fe(II) verdoheme−HmuO. This is different from the reported loss of the bound azide during crystallization and modification of the verdoheme group, during the synchrotron diffraction measurements of rat verdoheme−HO-1 complex.[25]

The *C*2 crystal of the verdoheme−HmuO complex contains two protein molecules in the asymmetric unit (molecules A and B), and their overall structures are almost superimposable with those of the heme−HmuO complexes.[56] The two molecules of the verdoheme−HmuO complex have essentially the same conformation (root-mean-square deviation of Cα atoms in residues 7−212 is 0.432 Å), so that discussions below are made on molecule A unless otherwise stated. Electron density around verdoheme fits well with the model structure including all the substituents of the oxaporphyrin ring (Figure 2a). The F_o-F_c map (Figure 2b) clearly shows an axial ligation of the azide ion, and its coordination geometry (d_{Fe-N}: 2.3 Å, ∠(Fe−N−N): 111°) is similar to that in the azide-bound heme−HO-1 complex (d_{Fe-N}: 2.2 Å, ∠(Fe−N−N): 117°).[57] The azide ligand is directed toward the α-*meso* position as found in the dioxygen ligand of the oxy-heme−HmuO complex.[28] A water molecule (Wat233) is located within hydrogen bonding distance of the terminal nitrogen atom of azide (2.8 Å). The nearby water forms a distal pocket hydrogen bond network consisting of Arg 132, Asp136, Gly135, and a water cluster (Figure 2b). This water network in the verdoheme complex, which also exists without the azide ligand,[31] is essentially the same as that observed in the heme−HmuO complex.[56] This structural similarity strongly suggests that the verdoheme ring cleavage at the third step of HO catalysis proceeds through a mechanism similar to that of the first heme *meso*-hydroxylation, i.e., water-mediated activation of the Fe−OOH species.[4,29]

3.2. Theoretical Results of the QM/MM Mechanistic Study. To probe the detailed mechanism of the verdoheme ring opening by HO, we first examined the possible intermediates and found that the ring-OOH and bridged intermediates are much higher in energy compared with the Fe−OOH intermediate. Specifically, the singlet ring-OOH and bridged intermediates are about 18.3 and 72.0 kcal/mol higher than the singlet Fe−OOH (see Part II in the SI for details) at the UB3LYP(B2)/MM level. Therefore, we explored only those mechanisms nascent from

Scheme 4. (a) Orbitals and Their Occupations in the Ground State of FeOOH Verdoheme Complex; (b) Orbital Occupations for Other States of FeOOH Verdoheme Complex

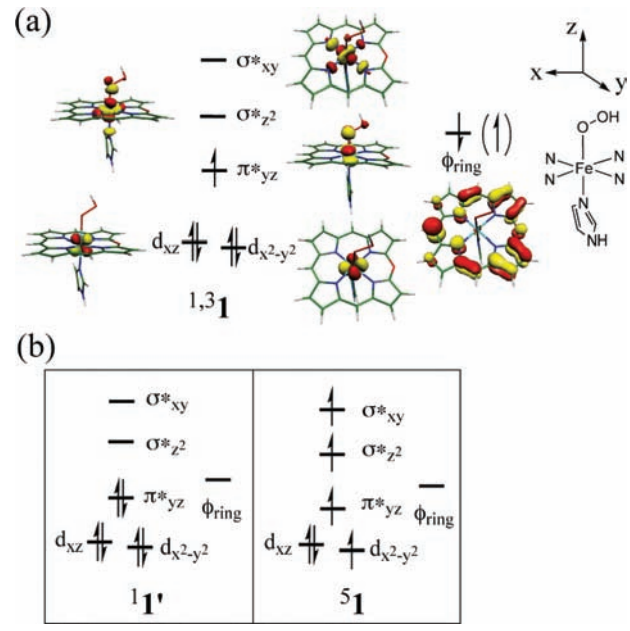

the $^{-}$OOH and HOOH bound ferrous verdoheme (FeOOH−verdoheme and FeHOOH−verdoheme) complexes, so-called the FeOOH pathway that is supposed to be formed during the O_2-supported reaction and the FeHOOH pathway that mimics the H_2O_2-supported reaction, respectively. Additionally, as we always recommend,[53] we ascertained here too that the full QM/MM barriers, and their trends, are dominated by the QM contribution (which involves the embedded MM charges), whereas the MM contribution is less than 4 kcal/mol. Details of the numerical results are summarized in the SI, while here we focus on the feasible mechanisms.

3.2.1. FeOOH Pathway. 3.2.1.1. FeOOH−Verdoheme Complex. As shown in Scheme 4, the FeOOH−verdoheme complex (**1**) possesses two electromers: one is a ferric hydroperoxide oxaporphyrin (OP) neutral radical, OP$^{\bullet}$Fe^{III}OOH, which has virtually degenerate open-shell antiferromagnetically and ferromagnetically coupled singlet and triplet states (^{1,3}**1** in Scheme 4a), and the other, a ferrous hydroperoxide oxaporphyrin cation, OP^{+}Fe^{II}OOH, has a close-shell singlet and quintet state (^{1}**1′** and ^{5}**1** in Scheme 4b), which is 3.2 and 4.9 kcal/mol higher in energy than ^{3}**1**, respectively. In Scheme 4a we show the orbitals and electronic configuration of ^{1,3}**1**, where the occupied π-type oxaporphyrin orbital is very similar to the singly occupied orbital in the *meso*-hydroxyheme species formed in the first heme degradation step.[14]

3.2.1.2. A Reaction Mechanism for the FeOOH Pathway. 3.2.1.2.1. Comparison of O−O Bond Breakage for the Singlet, Quintet, and Triplet Spin States. Starting from the FeOOH verdoheme complex (**1**), which can be either OP$^{\bullet}$Fe^{III}OOH or OP^{+}Fe^{II}OOH, the O−O bond breaking was found to be spin-state dependent, as described in Schemes 5 and 6. Scheme 5 shows the processes nascent from the singlet and quintet of **1**. These bond breakage processes of ^{1}**1** and ^{5}**1** were found to be homolytic (Scheme 5a and b), generating ^{1}OP$^{\bullet}$Fe^{IV}O[•OH] (tetraradicaloid configuration: $d_{x^2-y^2}{}^2\pi^*_{xz}{}^1\pi^*_{yz}{}^1\phi_{ring}{}^1\phi_O{}^1$) and ^{5}OP^{+}Fe^{III}O[•OH] (hexaradicaloid configuration: $d_{x^2-y^2}{}^1\pi^*_{xz}{}^1\pi^*_{yz}{}^1\sigma^*_{z^2}{}^1\sigma^*_{xy}{}^1\phi_O{}^1$) species, respectively. The mechanism for the close-shell singlet state involves heterolytic O−O bond breaking, followed by a proton

(56) Hirotsu, S.; Chu, G. C.; Unno, M.; Lee, D. S.; Yoshida, T.; Park, S. Y.; Shiro, Y.; Ikeda-Saito, M. *J. Biol. Chem.* **2004**, *279*, 11937–11947.
(57) Sugishima, M.; Sakamoto, H.; Higashimoto, Y.; Omata, Y.; Hayashi, S.; Noguchi, M.; Fukuyama, K. *J. Biol. Chem.* **2002**, *277*, 45086–45090.

Scheme 5. Mechanism for O−O Bond Cleavage in the FeOOH Pathway Starting from (a) Open-Shell Singlet, (b) Quintet, and (c) Close-Shell Singlet States[a]

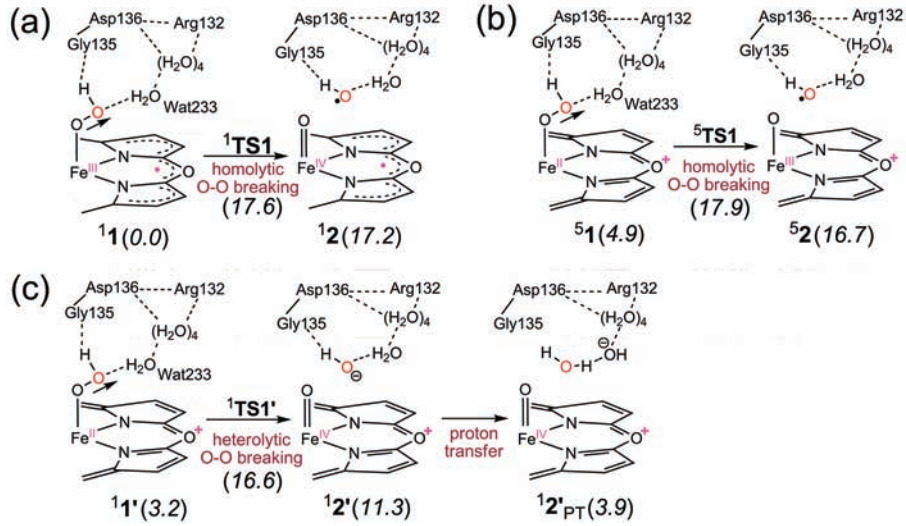

[a] Relative energies in parentheses correspond to UB3LYP(B2)/MM.

Scheme 6. Reaction Mechanism for the FeOOH Pathway on the Triplet Surface[a]

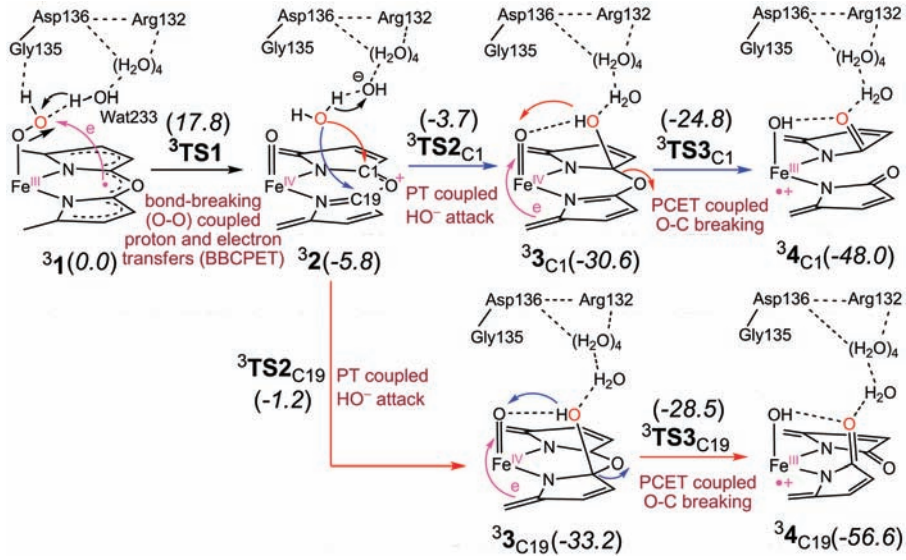

[a] UB3LYP(B2)/MM relative energies in parentheses.

transfer to form ^{1}OP$^+$Fe^{IV}O[O$_{dist}$H$_2$][O$_{Wat233}$H$^-$] (^{1}**2′**$_{PT}$). The resulting diradicaloid ^{1}**2′**$_{PT}$ involves singlet coupling of the electrons in the two Fe^{IV}O π* orbitals. The O−O cleavage on the triplet surface is significantly different and is shown in Scheme 6 later. However, before describing the triplet processes, it is instructive to first compare the relative energies of the three-spin-state mechanism, as depicted in Figure 3.

Figure 3 depicts the energy profile for this initial O−O bond cleavage on the three spin states. It can be seen that the TS energies for the three spin states are very close, 17−18 kcal/mol; however, while the triplet process is exothermic by 5.8 kcal/mol, the singlet (from open-shell singlet reactant) and quintet processes are endothermic by ca. 17 kcal/mol. Using B3LYP*, the TS energies for singlet and triplet are ∼3 kcal/mol lower than the B3LYP values. By contrast, for the quintet state, the TS energy is 3 kcal/mol higher than the B3LYP datum. As expected, B3LYP* tends to increase the energy gap between low-spin and high-spin states. This behavior is similar with our

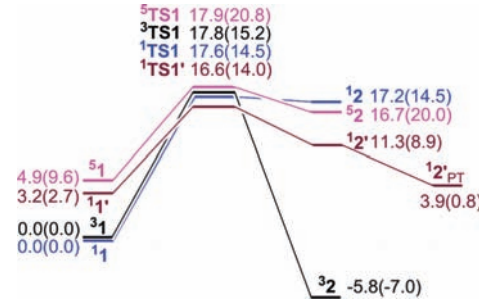

Figure 3. Calculated QM(B2)/MM energy profile (in kcal/mol) for the initial O−O bond breaking step in the FeOOH pathway. The relative energies are noted as B3LYP (B3LYP*) values.

recent findings for ferric heme species of allene oxide synthase.[58] In the close-shell singlet case, the ^{1}**2′** intermediate obtained by O−O bond heterolysis is not a real minimum. The OH anion abstracts a proton of Wat233 to form ^{1}**2′**$_{PT}$, which is still 9.7

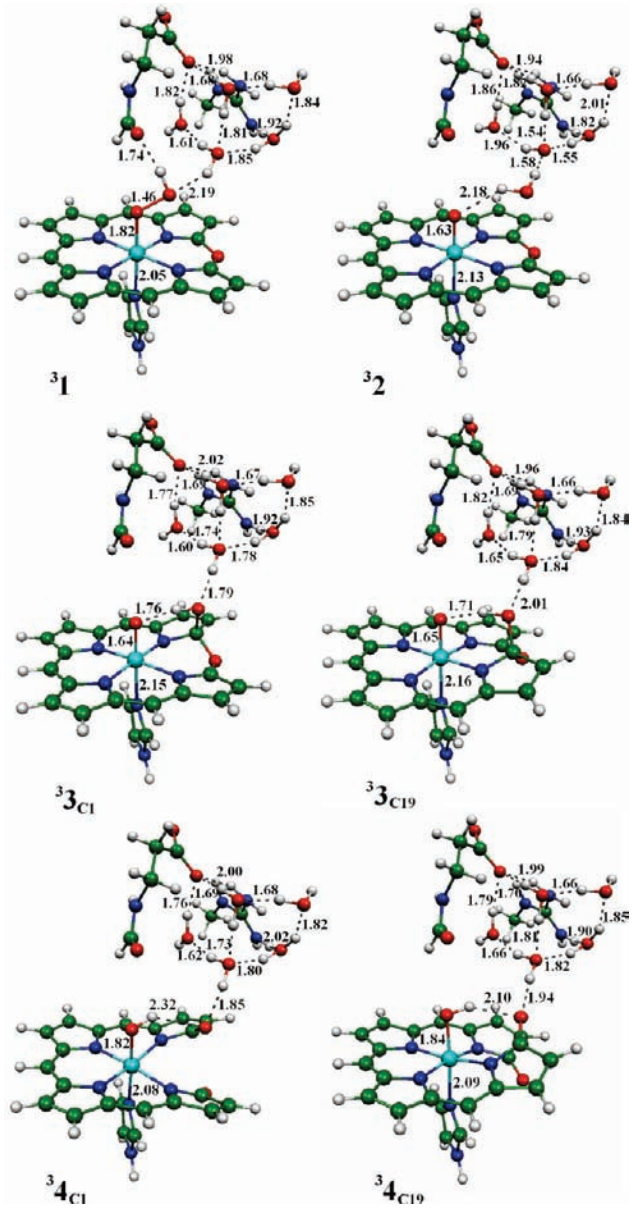

Figure 4. Key structures in the triplet-state FeOOH pathway shown in Scheme 5. **1** and **2** were optimized at the UB3LYP/B1a/MM level, while **3** and **4** were optimized at the UB3LYP/B1b/MM level.

kcal/mol higher than ^{3}**2**. In fact, the entire reaction mechanism starting from ^{1}**1′** is quite similar to that from ^{3}**1**. However, due to the higher energies of ^{1}**2′**$_{PT}$, this mechanism is relegated to the SI (Scheme S2). On the other hand, since the barriers of the reverse reactions back to ^{1}**1** and ^{5}**1** are very small compared with the forward O−O cleavage process, these intermediates will not accumulate, and in all likelihood, once formed they may either revert back to ^{1}**1** and ^{5}**1** or decay to the much more stable intermediate on the triplet surface. Thus it is deemed unnecessary to explore further these two spin states.

3.2.1.2.2. Complete Triplet-State Mechanism. Having verified that the process will be dominated by the triplet state, we turn now to inspect the corresponding mechanism in Scheme 6. The geometries of the key triplet structures for the entire mechanism are shown in Figure 4.

(58) Cho, K.-B.; Lai, W. Z.; Hamberg, M.; Raman, C. S.; Shaik, S. *Arch. Biochem. Biophys.* DOI: 10.1016/j.abb.2010.07.016.

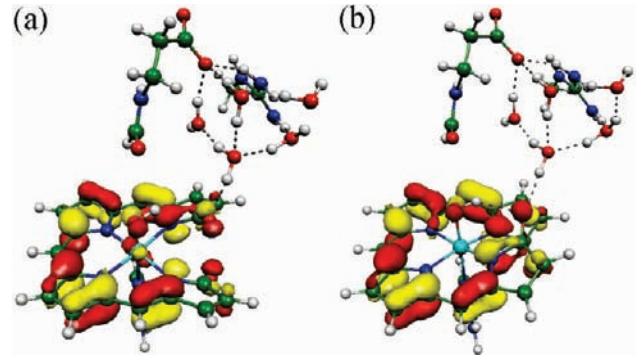

Figure 5. Singly occupied orbital of the ring of the Fe^{III}OH−BV$^{\bullet+}$ product (a) ^{3}**4**$_{C1}$ and (b) ^{3}**4**$_{C19}$.

As shown in Scheme 6, the O−O cleavage nascent from the triplet state ^{3}**1** is a process that involves O−O bond breaking coupled proton and electron transfers (BBCPET). The electron is transferred from oxaporphyrin to the departing $O_{dist}H$ moiety, leaving behind an Fe^{IV}O complex with a triplet $\pi^*_{xz}{}^1\pi^*_{yz}{}^1$ configuration. The departing $O_{dist}H$ hydroxide anion concomitantly abstracts a proton from the nearby H-bonded water molecule (Wat233) in the water cluster, thus resulting in the intermediate ^{3}**2**, ^{3}OP$^+$Fe^{IV}O[$O_{dist}H_2$][$O_{Wat233}H^-$]. Inspection of the structure of ^{3}**2** (see Figure 4) shows that the water cluster claws the $O_{Wat233}H^-$ anion via strong hydrogen bonds, and as such, the resulting $O_{Wat233}H^-$ species can be viewed as a strong base stored in the distal water cluster. From here, the reaction bifurcates into two different pathways, which lead to ^{3}**4**$_{C1}$ and ^{3}**4**$_{C19}$, as depicted in Scheme 6.

Thus, as shown in Scheme 6, the cluster-embedded $O_{Wat233}H^-$ species can act as a base catalyst that renders the water molecule, $HO_{dist}H$, more nucleophilic by pulling one of its protons. In turn, the charged HO_{dist} moiety can perform nucleophilic attacks on either C1 or C19, the carbon atoms adjacent to the oxygen atom of oxaporphyrin. These processes produce hydroxyl-oxaporphyrin, ^{3}[(OP−OH)Fe^{IV}O], ^{3}**3**$_{C1}$, or ^{3}**3**$_{C19}$. Subsequently, the ^{3}**3** species undergo proton transfers, from the hydroxyl groups on C1 and/or C19 to the Fe^{IV}O moiety, which are coupled to electron transfers (PCET) from macrocycle to the Fe^{IV}O moiety, and to simultaneous ring openings (bond breaking). The so-generated ^{3}**4**$_{C1}$ and ^{3}**4**$_{C19}$ species correspond to Fe^{III}OH biliverdin cation radicals (Fe^{III}OH−BV$^{\bullet+}$), which will ultimately be converted to Fe(II)−biliverdin by accepting 2e$^-$ and one H$^+$. Figure 5 shows the ring singly occupied orbitals of BV$^{\bullet+}$ for the ^{3}**4**$_{C1}$ and ^{3}**4**$_{C19}$ species, while Figure 6 shows the complete energy profiles. We note that the antiferromagnetic counterpart of ^{3}**4** (the single π^*_{yz} electron is antiferromagnetically coupled to the electron of BV$^{\bullet+}$), ^{1}**4′** nascent from ^{1}**1′**, is very close in energy (see Scheme S2 in the SI) to ^{3}**4**. However, as we already stated, ^{1}**2′**$_{PT}$ lies 9.7 kcal/mol above its triplet coupling counterpart, ^{3}**2**, and hence this spin-state mechanism is not considered in detail. In summary, it is clear that the rate-limited step in the FeOOH pathway is the first O−O bond-breaking step, with a barrier of 17.8 kcal/mol on the triplet surface.

3.2.2. FeHOOH Pathway. 3.2.2.1. FeHOOH−Verdoheme Complex. The singlet, triplet, and quintet spin states of the FeHOOH−verdoheme complex (**1-H**) were investigated and were all found to possess the ferrous hydroperoxide oxaporphyrin cation OP$^+$Fe^{II}HOOH electronic structure, shown in Scheme 7. All attempts to obtain the oxaporphyrin radical state like ^{1,3}**1** in the FeOOH−verdoheme complex failed. Two conformations of the ^{1,3,5}**1-H** were found, and we focus herein

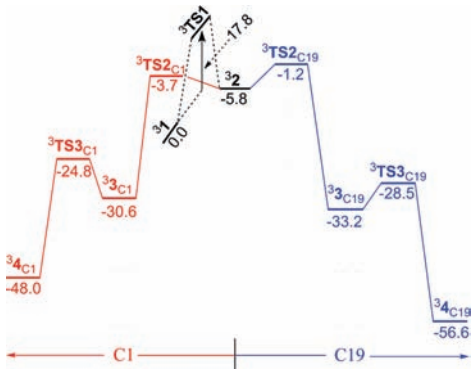

Figure 6. Calculated energy profile (in kcal/mol) for the FeOOH pathway in the triplet surface from ^{3}**2** to product (^{3}**4**$_{C1}$ and ^{3}**4**$_{C19}$) at the UB3LYP(B2)/MM level. The protruding little profile for ^{3}**1**→^{3}**2** shows the barrier for O−O cleavage taken from Figure 3.

Scheme 7. (a) Orbitals and Their Occupations in Singlet FeHOOH−Verdoheme Complexes, ^{1}**1-H**; (b) Occupancy Diagrams of ^{3,5}**1-H**

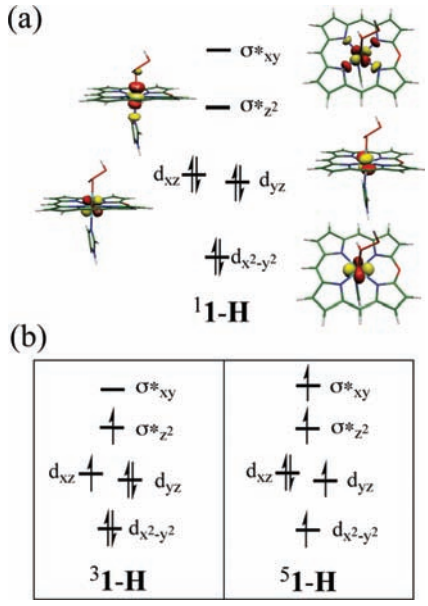

on the most stable one for each spin state, while the other is relegated to the SI. In the choice conformation, the ground state was found to be the close-shell singlet state (^{1}**1-H** in Scheme 7), while the triplet and quintet states are 3.9 and 1.5 kcal/mol higher at the UB3LYP(B2)/MM level, respectively. As might be expected, the Fe−O bond distance of the FeHOOH−verdoheme complex, ^{1}**1-H**, is longer than that in the corresponding FeOOH−verdoheme complex (^{3}**1** in Figure 4 vs ^{1}**1-H** in Figure 7).

3.2.2.2. Computed Reaction Mechanism. Unlike in FeOOH, here with the FeHOOH, the singlet and triplet spin state energy profiles run closely in energy almost throughout the pathway and exhibit the same mechanism. The corresponding computed mechanism is described in Scheme 8, while Figure 7 shows the structural details of the participating species. Figures 8 and 9 summarize the computed energy profiles. We shall present this wealth of data in order.

As shown in Scheme 8, the FeHOOH−verdoheme complex (^{1,3}**1-H**) undergoes O−O bond homolysis, which leads to ^{1,3}**2-H**, corresponding to $OP^+Fe^{III}OH^-$[•OH], wherein the OH radical is hydrogen bonded (H-bonded) to Gly135 and to Wat233 which is part of the water cluster (consult Figure 7). Subsequently, the OH radical flips and switches H-bonding partners to the FeOH moiety in ^{1,3}**3-H**. This flip, along with the conformational changes of the H-bonding network, suitably orients the OH radical for attack on the carbon positions C1 and C19, adjacent to the oxygen atom of oxaporphyrin, and thereby forms ^{1,3}**4-H**. Subsequently, the proton of the hydroxyl group on C1 and C19 is transferred to the FeOH moiety to generate ^{1,3}**5-H**. This is followed by O−C bond breaking, leading to the formation of the water bound Fe^{III}−biliverdin cation radical species ($Fe^{III}OH_2$−$BV^{\bullet+}$) ^{1,3}**6-H**.

Turning now to Figures 8 and 9, we note a few important features:

(a) Similar to the FeOOH pathway, here too the rate-limiting step is the O−O bond breakage. Here the mechanism is apparently different for the two spin states, and as shall be analyzed later, this is due to the electronic structure differences of the two states (see Scheme 7). Note that the barrier on the triplet state is very small, compared with the one for the FeOOH pathway.

(b) Past this step, at **2-H**, the two spin states attain the same electronic configuration on iron, $d_{x^2-y^2}{}^2(\pi^*_{xz}/d_{yz})^3$ wherein the single π^* electron is ferro-/antiferromagnetically coupled to the electron of the departing OH radical. Consequently, the two spin states from **2-H** onward to **6-H** (Figure 9) coalesce, and the QM/MM calculations (Figure 8) show a singlet−triplet two-state reactivity (TSR).[59] Note also that the energy profile from **2-H** onward is a downhill roll with very small barriers en route to the final state **6-H**.

4. Discussion

The X-ray crystallography reported herein reveals a sizable water cluster in the distal pocket of the Fe(II) verdoheme complex of HmuO. Since the distal-water cluster was shown previously[14] to play a major role in the hydroxylation of the heme by HO, the new structural data enabled us to unify the description of the heme degradation steps by means of QM/MM calculations and to unravel the mechanism for the conversion of verdoheme to biliverdin (Scheme 1). The QM/MM calculations support the previous experimental results[20] that the degradation of verdoheme to biliverdin can be supported by both O_2 and H_2O_2 and that the H_2O_2 path is more effective (here, a lower barrier for the O−O cleavage). Thus, the QM/MM results are in accord with experimental facts.

However, the QM/MM calculations provided additional essential insight that is typical for the theoretical atomistic calculations. Thus, QM/MM calculations revealed the identity of the complexes that initiate the degradation processes as FeOOH and FeHOOH, specified the O−O cleavage nature of the rate-controlling step, and demonstrated the essential role of the water cluster. Additionally, the QM/MM calculations underscored the key differences between the respective O−O bond cleavage reactions for the O_2- and H_2O_2-supported reactions. The following discussion will focus on the rate-controlling steps of the two pathways and on the role played by the water cluster.

4.1. O−O Bond Cleavage. The O−O bond cleavage process is the rate-limiting step in both FeOOH and FeHOOH pathways. As mentioned above, the mechanism of this step is quite different in the FeOOH and FeHOOH pathways. Focusing on

(59) Schröder, D.; Shaik, S.; Schwarz, H. *Acc. Chem. Res.* **2000**, *33*, 139–145.

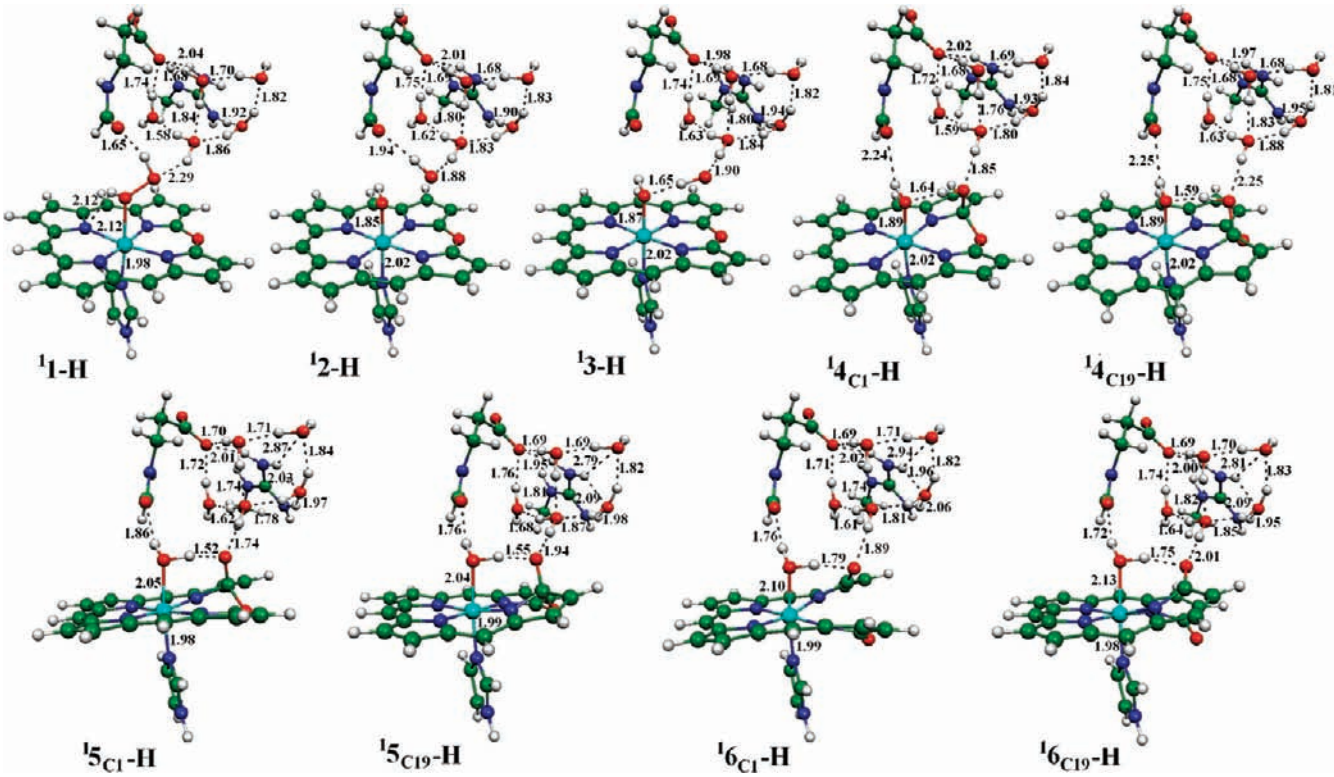

Figure 7. Optimized singlet state structures for reactions shown in Scheme 7. The corresponding triplet state species are similar and are relegated to the SI.

Scheme 8. Reaction Mechanism for the FeHOOH Pathway Nascent from ^{1,3}**1-H**

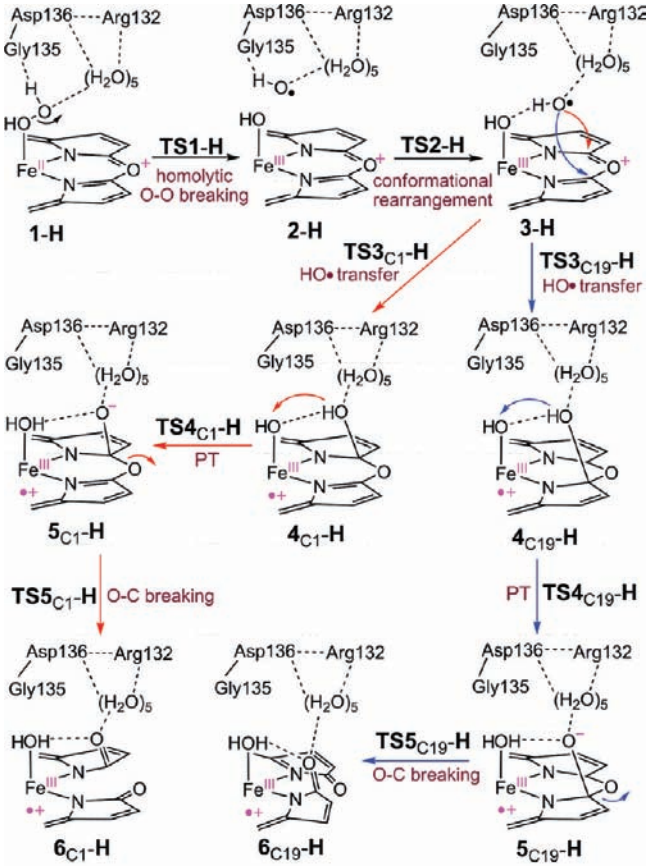

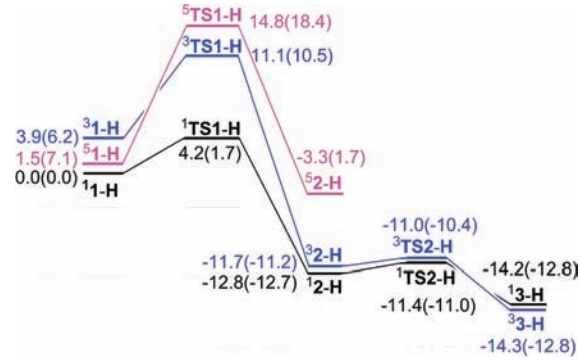

Figure 8. UB3LYP(B2)/MM energy profile for the Fe−HOOH pathway (in kcal/mol) from **1-H** to **3-H**. The relative energies are noted as B3LYP (B3LYP*) values.

the lowest-energy processes, in Scheme 6 vs 8, one can see that the FeOOH pathway involves a complex O−O reaction leading from ^{3}**1** to ^{3}**2**, while the FeHOOH pathway involves two essentially homolytic processes from both ^{1}**1-H** and ^{3}**1-H** with the latter having a significantly smaller barrier (see Figure 8). In addition, the processes nascent from ^{3}**1** involve Fe^{III} while the one from ^{1}**1-H** and ^{3}**1-H** involve Fe^{II}. Thus, there should be similarities as well as differences with the O−O bond cleavages in the first HO step (Scheme 1) and in P450 or other heme enzymes, where the process is initiated from a low-spin Fe^{III}−OOH (or Fe^{III}−HOOH).

As noted in the description of the process in Scheme 6, the O−O bond cleavage, in the FeOOH pathway, involves bond-breaking coupled proton and electron transfers (BBCPET), whereby an electron originally delocalized in the macrocycle of verdoheme is transferred to the O−O bond, while Wat233, a member of the water cluster, protonates the nascent OH^-. The

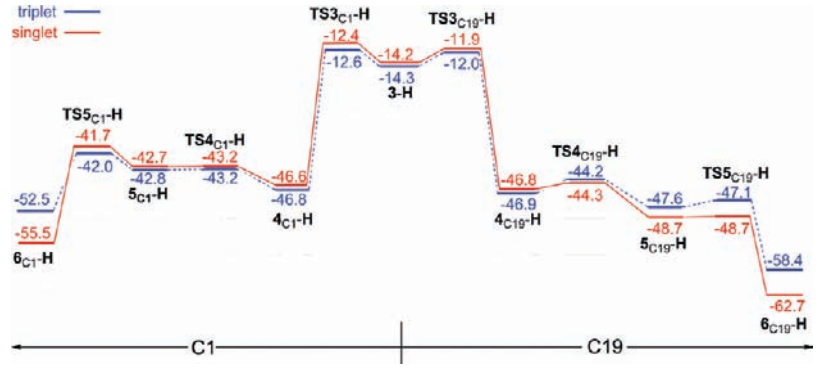

Figure 9. UB3LYP(B2)/MM energy profile for the Fe−HOOH pathway on the singlet (red) and triplet (blue) surface from **3-H** to products ($\mathbf{6}_{C1}$**-H** and $\mathbf{6}_{C19}$**-H**).

Scheme 9. (a) Events Occurring during O−O Bond Breaking of ^{3}**1**; (b) Key Orbitals of ^{3}**1** and Electronic Occupancy Evolution during the Process

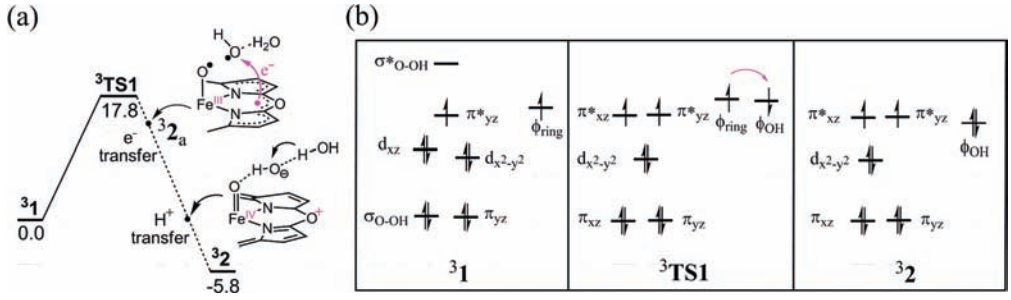

QM/MM calculations show however that these events do not occur synchronously, but consecutively as described in Scheme 9.

Scheme 9a shows the sequence of events past ^{3}**TS1** that involves essentially O−O homolysis. Thus, on the way down, there occurs an electron transfer from oxaprophyrin to the departing OH radical to form $^3\mathbf{2}_a$, followed by the proton transfer that generates the final ^{3}**2** species. Scheme 9b describes the electronic structure changes along these phases: Initially ^{3}**1** has an $Fe^{III}(d^5)$ configuration; one of the orbitals labeled as π^*_{yz} involve FeO antibonding interaction, and it possesses a matching bonding orbital, π_{yz}, which describes an FeO π-bonding. The O−OH bond has a corresponding filled σ_{O-OH} and vacant σ^*_{O-OH} orbital pair. In addition, the oxaprophyrin of verdoheme has an odd electron in the orbital ϕ_{ring}. As the bond is homolized in ^{3}**TS1**, the $\sigma_{O-OH}^2/\sigma^*_{O-OH}{}^0$ pair is converted to a singly occupied $\phi_{OH}{}^1$ located at the departing HO• radical and a $\pi_{xz}{}^2/\pi^*_{xz}{}^1$ pair which arises by overlap of the nascent oxygen radical on Fe^{III}−O• with the d_{xz} iron orbital. Past the TS species an electron is shifted from ϕ_{ring} to ϕ_{OH}, thereby generating $^3\mathbf{2}_a$, wherein the departing OH has become a hydroxide anion. At this point, Wat233 from the cluster relays a proton to the nascent OH^- and generates, finally, the intermediate ^{3}**2**, $^3OP^+Fe^{IV}O$-$[O_{dist}H_2][O_{Wat233}H^-]$. This is quite a unique net-heterolytic O−O bond cleavage process. In its homolytic stage (up to ^{3}**TS1**) it resembles the first HO step[14] which is initiated by the doublet Fe^{III}OOH complex, while in its electron-transfer-assisted stage, it resembles the process in P450cam[60] and chloroperoxidase (CPO)[61] wherein the porphyrin transfers an electron to the departing OH and causes its protonation and formation of Compound I. The calculated barrier for this HO step (17.8 kcal/mol) is in between the two barriers 20 kcal/mol for the first HO step and ∼15 kcal/mol for P450.

As discussed above in Scheme 7 the added proton in **1-H** generates a close-shell Fe^{II}−HOOH complex, wherein the oxaporphyrin ligand of verdoheme is a cation. This is consistent with the weaker σ electron-donor capability of HOOH, as the sixth ligand of iron, compared with $^-$OOH, and is probably the root cause why the verdoheme does not transfer an electron to the departing OH radical as found for the FeOOH pathway.

The orbital occupancy during the O−O cleavage in the FeHOOH path is illustrated in Scheme 10 in the singlet (a) and triplet (b) states. Inspection of Scheme 10a reveals that the O−O homolysis transforms the initial $\sigma_{O-O}{}^2/\sigma^*_{O-O}{}^0$ pair of ^{1}**1-H** to a singly occupied $\phi_{OH}{}^1$ on the departing OH radical and an in-plane p-orbital on the oxygen of the FeOH moiety, which gains one electron from $d_{xz}{}^2$ and becomes an in-plane lone-pair (p_x). This reorganization generates Fe^{III}−OH with a d-block electronic configuration $d_{x^2-y^2}{}^2d_{yz}{}^2\pi^*_{xz}{}^1$ which is antiferromagnetically coupled to the departing OH radical. This electronic structure of the TS continues down to the intermediate, ^{1}**2-H**, with relaxation of the orbitals but without change in their natures. The very low energy of the TS for this process is quite unusual, and it is about 14 kcal/mol lower that in the FeOOH pathway (4.2 vs 17.8 kcal/mol with B3LYP, 1.7 vs 15.2 kcal/mol with B3LYP*). However, if we compare this process to the analogous one in the first HO step, the finding is no longer surprising. In the first hydroxylation step,[14] the barrier for O−O bond cleavage of the Fe^{III}OOH complex (20.0 kcal/mol) is also much higher than that for the Fe^{III}HOOH complex (11.0 kcal/mol, from the quartet ground state). Additionally, compared with the doublet Fe^{III}HOOH reactant, in the first heme-degradation step,[14] the O−O bond cleavage process is exothermic by 2.8 kcal/mol with

(60) Zheng, J.; Wang, D.; Thiel, W.; Shaik, S. *J. Am. Chem. Soc.* **2006**, *128*, 13204–13215.
(61) (a) Chen, H.; Hirao, H.; Derat, E.; Schlichting, I.; Shaik, S. *J. Phys. Chem. B* **2008**, *112*, 9490–9500. (b) Lai, W. Z.; Chen, H.; Cho, K.-B.; Shaik, S. *J. Phys. Chem. A* **2009**, *113*, 11763–11771.

Scheme 10. Orbital Occupancy during O−O Cleavage for **1-H** in the (a) Singlet and (b) Triplet States

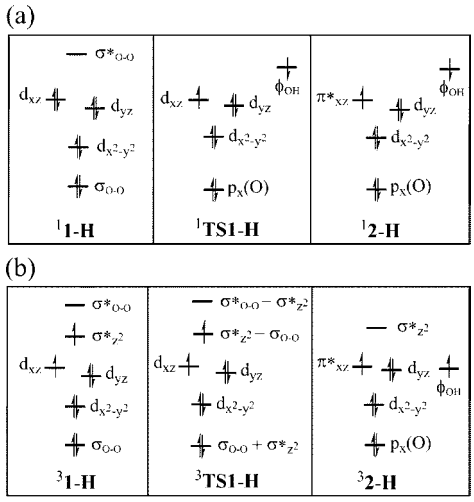

a barrier of 8.2 kcal/mol, while here, in the third heme-degradation step, the O−O bond cleavage of the $Fe^{II}HOOH$ verdoheme complex is more exothermic, ca. −13.5 kcal/mol. Therefore, according to the Bell−Evans−Polanyi principle, it is entirely expected that the barrier for the O−O cleavage from the verdoheme−FeHOOH complex (**1-H**) will be lower than the corresponding barrier in the porphyrin−$Fe^{III}HOOH$ complex.

By contrast to the process nascent from the singlet state, as seen from Scheme 10b, the electronic structure of ^{3}**1-H** involves one electron in the $\sigma^*_{z^2}$ orbital, whereas the electronic structure of ^{3}**2-H** involves a $d_{x^2-y^2}{}^2 d_{yz}{}^2 \pi^*_{xz}{}^1$ FeOH configuration which is ferromagnetically coupled to the departing OH radical $\phi_{OH}{}^1$. This means in turn that the $\sigma^*_{z^2}$ orbital will have to be vacated during bond cleavage, and this requires some overlap between the $\sigma^*_{z^2}$ orbital and $\sigma_{O-O}/\sigma^*_{O-O}$ orbtials, as reflected in the electronic structure of ^{3}**TS1-H**, which shows still a single electron in a mixed $\sigma^*_{z^2}-\sigma_{O-O}$ orbital. Keeping this excited electronic configuration contributes to one factor for the higher energy of ^{3}**TS1-H** compared to the singlet state species. The other factor is the deformation energy of the FeHOOH moiety required to mix the orbitals, which can be easily seen from the increased shortening of the Fe−O bond and the deformation of the ∠FeOO angle for the triplet state. Thus, in the ^{3}**TS1-H**/^{1}**TS1-H**, the Fe−O bond length shortens by 0.32/0.22 Å and the ∠FeOO angle increases by 11.6°/1.3° (Figure S22 vs S23), compared with the values for ^{3}**1-H**/^{1}**1-H**.

4.2. Functions of the Crystal Waters in the Distal Pocket. Much like the first heme degradation step,[14] in this study too, the crystal waters in the distal pocket play an important role in the third heme degradation step of HO catalysis. The distal water cluster functions as a whole species, and specifically through the water molecule (Wat233) closest to the Fe(H)OOH moiety. Thus, in the FeHOOH pathway, which bears similarity to the first heme degradation step, the distal water cluster stabilizes the produced OH radical by a strong hydrogen bond (from Wat233) and thus controls the movement of the OH radical to facilitate subsequent attack on the α-pyrrole positions of α-meso edge of the oxaporphyrin ring. However, in the FeOOH pathway, which involves OH^- generation (see Schemes 6 and 9), the water cluster acts as a proton source. Specifically, Wat233 plays a dual role: it acts first as a proton donor, which protonates the departing OH^-, and then as a proton acceptor that regenerates OH^-, when it is required to nucleophilically attack C1 and/or C19 of the verdoheme. In other words, Wat233 and the entire water cluster act as a shuttle that can stabilize a strongly nucleophilic OH^- moiety and can deliver it to the α-pyrrole carbons. Thus, the distal water cluster fixes and insulates a highly nucleophilic reagent OH^- via strong H-bonds and through the to-and-fro proton shuttles. *As such, it functions as a strategic biocatalyst during the entire heme degradation process.*

5. Conclusions

The combination of theoretical and X-ray crystallographic approaches, brought to bear on the enigmatic mechanisms of the third oxidation step in heme degradation (Scheme 1) by the enzyme HO, elucidates the mechanism and provides a great deal of insight into this vital process. The X-ray structure of the azido complex of Fe(II)−verdoheme clearly showed the presence of a cluster of six water molecules hovering over the Fe−azide moiety. The QM/MM calculations, initiated from this structure by replacing azide with either HOO^- or H_2O_2, indicate that the initial O−O bond breaking step is the rate-determining step in the ring-opening transformation for both FeOOH−verdoheme and FeHOOH−verdoheme complexes. The FeHOOH pathway has an extremely low barrier (only 4.2 kcal/mol), indicating in accord with experiment[20] that the FeHOOH−verdoheme complex is more reactive than the FeOOH−verdoheme complex. The transition states for O−O bond breakage in the two mechanisms are dominated by bond homolysis. However, in the FeOOH−verdoheme path, the bond homolysis is further coupled to electron transfer (from the verdoheme to the departing OH) and proton transfers to and from the Wat233 member of the water cluster, thus enabling a nucleophilic OH^- attack on one of the α positions of the C1−O−C19 bay of verdoheme. By contrast, the FeHOOH−verdoheme path is purely homolytic, wherein the departing OH• radical attacks the C1−O−C19 bay.

The water cluster in the distal pocket was found to play a major role in the degradation mechanism: (i) it stabilizes highly reactive OH^-/OH• species, and (ii) it orients them for a regiochemical attack on one of the α positions of the C1−O−C19 bay of verdoheme. Thus, in the FeOOH−verdoheme pathway, the cluster stabilizes the highly basic OH^- species, which then catalyzes the nucleophilic attack of a water molecule on the C1−O−C19 bay. Similarly, in the FeHOOH pathway, the water cluster claws by hydrogen bonds the OH radical and directs the movement of the radical so as to facilitate the eventual attack on the oxaporphyrin ring. It is likely that the cluster also shuttles the protons required for the final freeing of the iron ion from the ring-opened biliverdin. Thus, as in the previously studied first oxidation step of heme degradation,[14] here too the water cluster acts as a strategic biocatalyst.

Acknowledgment. This work was supported by the Israel Science Foundation (ISF 53/09 to S.S.), Grants-in-Aid for Scientific Research (17GS0419, 18370052, and 21350087 to M.I.S.; 18770103, and 20750125 to T.M., and 18770080 and 20770076 to U.M.) from JSPS and MEXT, Japan. The synchrotron radiation experiments at Photon Factory were conducted under the approvals 2007G515 and 2007G516.

Supporting Information Available: Complete citations for refs 32, 36, 40, and 52 as well as spin distribution, energies, geometries of all the structures and discarded pathways. This material is available free of charge via the Internet at http://pubs.acs.org.

JA104674Q